

Automatic 3D Model Acquisition for Unknown Objects based on Hybrid Vision Technology

Wei Fang¹, Lianyu Zheng^{1,#}, Bingwei He², Qing Wang³

¹ School of Mechanical Engineering and Automation, Beihang University, Xueyuan road, HaiDian region, Beijing, China, 100191

² School of Mechanical Engineering and Automation, Fuzhou University, Xueyuan road, MinHou region, Fuzhou, China, 350116

³ School of Engineering and Computing Sciences, Durham University, South Road, Durham DH1 3LE, United Kingdom

Corresponding Author / E-mail: lyzheng@buaa.edu.cn, TEL: +86-010-8231-7725, FAX: +86-010-8231-7725

KEYWORDS : 3D modeling, Viewpoint planning, Hybrid vision technology, Binocular structured light system

Abstract: Three-dimensional (3D) model acquisition is the process of building a 3D model of an object. But due to the limited field of view of the scanner, this task is mainly performed by taking several scans with human intervention. In order to make the 3D modeling process efficient, a novel automatic 3D modeling method for unknown object based on hybrid vision technology in a binocular structured light system (BSLS) is proposed. Firstly, the limit visual vacuums of the BSLS are established, and they will be used to predict the unknown area with an acquired 2.5D range image. With the 2D gray image acquired synchronously, the coarse boundary size is recovered from Shape from Shading, and it leads the prediction of the unknown area to be more precise. Based on the combination of the predicted contours, the next best viewpoint is determined with more unknown areas visible. The proposed method can be used to obtain the 3D model of unknown objects automatically and completely, and the experimental results illustrate the validity and efficiency of our approach.

1. Introduction

Three-dimensional (3D) models of real objects are used in many applications, such as manufacturing engineering, object manipulation, virtual reality and augmented reality, et al, and the 3D model acquisition methods are widely studied attributes of computer vision technology¹. However, due to their limited fields of view, the scanners must be placed at different locations for a complete 3D model acquisition²⁻⁵. The human operation is the mainstream method for viewpoints selection, as in the Michelangelo Project⁶, which made the 3D model acquisition a very tedious and time-consuming task and the modeling quality dependent on the skill of the operator.

In order to perform the automatic 3D model acquisition, the viewpoints of the scanner are better determined automatically. Many researchers have made great efforts on this issue. Blaer et al.⁷ proposed a method that determined the next best viewpoint from a set of candidates, where the computation time is reduced by means of looking for just one type of voxel. However, they divided the modeling process into initial and second scans, which made the 3D model acquisition complicated. Other work was that of Callieri et al.⁸ and Larsson et al.⁹, both of their work used an industrial robot in combination with a turntable to model the objects. The former focused on 3D modeling, but did not consider path planning aspects at all. For the latter, the user needed to manually input object size and stand-off distance for each object individually, which did not render the system autonomous. Vasquez-Gomez et al.¹⁰ proposed a search-

based paradigm to generate a set of candidate viewpoints. With the modeling constraints of new information, positioning, sensing and registration, the best one was determined by the evaluation of all candidates. He et al.¹¹ proposed a new concept of limited visible surface in the laser scanning system, according to unknown space prediction, where the next best view is determined with the maximum predicted surface visible. However, due to the lack of flip degrees of freedom, the top surface of the object cannot be modeled. Torabi et al.¹² chose the next best viewpoint from a set of candidates in the workspace of the manipulator arm, and then inverse kinematics was addressed to match the desired sensor location in the workspace. The novelty of the method was the generation of the candidates and the stop criteria. Nevertheless, it assumed the bounding box of the object as a priori, and did not consider the estimation of the unknown area.

To overcome the limitation of the above automatic 3D modeling methods, the multi-sensor or multi-method fusion technology provides another alternative in automatic 3D modeling for their robust performances. Martins et al.¹³ presented a method to automate the process of 3D scanning using range sensors and based on a priori known information from a CAD model, but the dependence on the CAD model lowered its applicability. Sablatnig et al.¹⁴ and Sun et al.¹⁵ presented an automatic 3D modeling strategy based on active and passive vision technology. They obtained the coarse contour from the intersection of a target object border in images, which were acquired from different viewpoints. And then, according to the complexity of the contour already obtained, the viewpoints around the target object were arranged by a suitable step length. But the

approaches were not suitable for nonconvex objects, and the determination of the step length would produce a large amount of redundant information. Fang et al.¹⁶ proposed a sensor fusion method in a BSLS for automatic 3D reconstruction for an object, but the next best viewpoint was only considered by different rotation positions. Due to the lack of translation, the method is only suitable for small objects. Based on the surface-based and volumetric-based method, Kriegel et al.¹⁷ proposed an efficient autonomous 3D reconstruction of the unknown objects with laser scanning and an industrial robot. The candidate viewpoints were iteratively determined by the combination of boundary detection and trend surface estimation. However, the trend surface estimation was not deemed to be robust, with some mutation of the surface, and it may lead the next best viewpoint estimation to fail.

In summary, despite the achievements obtained above, the specific equipment requirements, such as industrial robots, may limit their practical application for the higher cost and space restriction on site, and the laser scanning system is not fast enough for 3D scanning. With the benefits of high efficiency and low cost, the BSLS, as shown in Fig. 1, is widely used. But to our knowledge, most attention of the BSLS is paid to the goal of gaining the 2.5D range image of the object, and the 2D gray image is ignored. In this paper, the 2.5D range image and 2D gray image, being acquired synchronously in a scanning process, are made full use of for automatic 3D modeling through the hybrid vision technology. Firstly, based on the active vision for a 2.5D range image acquisition, the limit visual vacuums of the BSLS are built. In addition, the coarse boundary size of the unknown object can be recovered from a 2D gray image with passive vision SFS¹⁸⁻¹⁹ (Shape from Shading). Combining the boundary size from passive vision and the limit visual surface from active vision, a more accurate unknown area can be predicted. Finally, the scanning viewpoint with more unknown visual areas is deemed the next best one, which can be generated automatically for the complete 3D model acquisition.

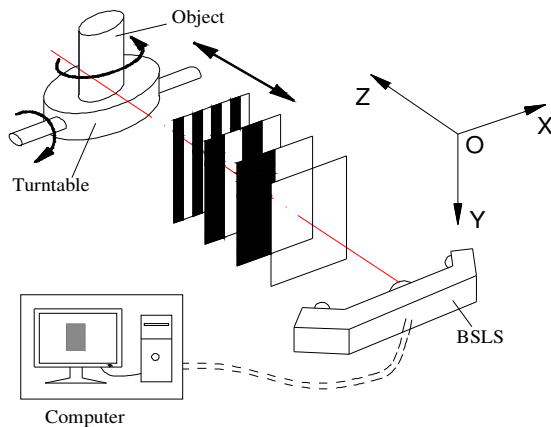


Fig. 1 Schematic of the BSLS experimental platform

The remainder of this paper is organized as follows. In section 2, the hybrid vision technology of the BSLS is introduced. Section 3 describes the automatic 3D model acquisition strategy b viewpoint planning. In Section 4, an example for a complete 3D model acquisition is presented. We conclude the paper with some discussions in Section 5.

2. Hybrid Vision Technology in BSLS

Based on the hybrid vision technology in a BSLS, the overall flowchart of automatic 3D modeling is depicted in Fig. 2.

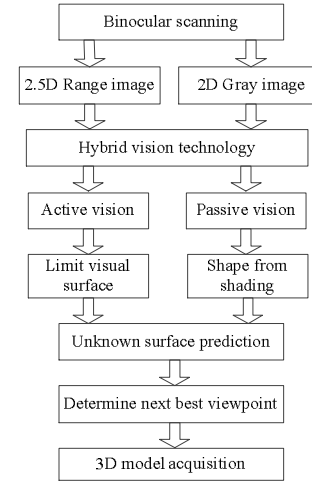


Fig. 2 The overall flowchart of automatic 3D model acquisition

2.1 Active vision prediction strategy

2.1.1 Side surface prediction

To obtain the effective DOF (depth of field) of the BSLS, a flat plane with high precision is measured under different DOF as a reference. Within a certain flatness threshold of 0.05mm, the measured DOF is considered to be effective when the fitting accuracy is located. Repeating the above process at different depths, the DOF range of the BSLS can be obtained. As illustrated in Fig. 3, the DOF d_i is acquired by moving the reference planar along the z axis, and the effective range $d_i \in [d_{\min}, d_{\max}]$ can be obtained.

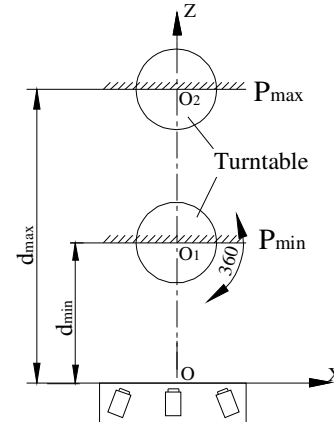


Fig. 3 DOF acquisition schematic of the BSLS

Within the range of the acquired DOF, the left limit visual angle θ_l , denoting the critical position of the reference plane, visual or not, is obtained by the angle between the normal vector \vec{n}_{il} of the planar and the negative direction of the z axis (shown in Fig.4). The right limit visual angle θ_{ir} can also be obtained in the same way. Based on the visibility principle, with only the normal vector $\vec{n}_{il}(\vec{n}_{ir})$ of the surface patch located in the limit visual angle, these surface ones are considered as visible.

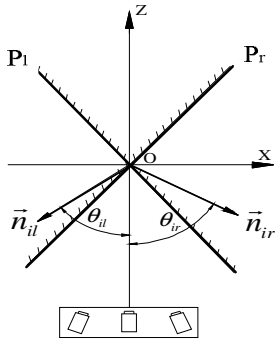


Fig. 4 The limit visual rotation angle of BSLS

Repeating the above process at different d_i within the DOF range, a series of left (right) limit visual angles $[z_i \ \theta_{il}][z_i \ \theta_{ir}]$ are collected. The corresponding relationship between the limit visual angle $\theta_{il}(\theta_{ir})(rad)$ and $z(mm)$ can be yielded with least squares, as equations (1) and (2) show, respectively.

$$\theta_{il} = \begin{cases} 0.0018z - 0.1602 & 570 \leq z \leq 680 \\ 1.0421 & 680 \leq z \leq 780 \end{cases} \quad (1)$$

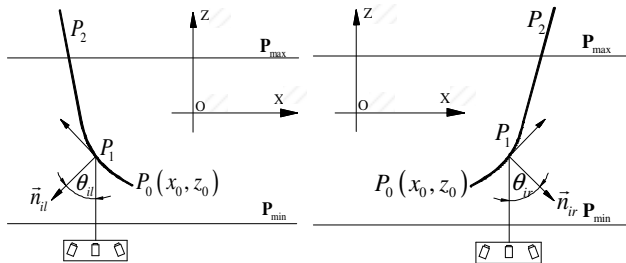
$$\theta_{ir} = \begin{cases} 0.0017z - 0.1382 & 570 \leq z \leq 680 \\ 1.0348 & 680 \leq z \leq 780 \end{cases} \quad (2)$$

Therefore, according to equations (1) and (2), the left and right limit visual curves can be built logically, which are illustrated in equation (3) and equation (4), respectively.

$$\begin{cases} x_l = 555.6 \ln \left(\sin \left(\frac{z-89.0}{555.6} \right) \right) + C_1 & 570 \leq z \leq 680 \\ z = -1.71x + C_2 & 680 \leq z \leq 780 \end{cases} \quad (3)$$

$$\begin{cases} x_r = 588.2 \ln \left(\sin \left(\frac{z-81.3}{555.6} \right) \right) + C_3 & 570 \leq z \leq 680 \\ z = 1.68x + C_4 & 680 \leq z \leq 780 \end{cases} \quad (4)$$

With the projected boundary point of the acquired 2.5D range image on the XOZ plane, the $C_i (i=1,2,3,4)$ in equations (3) and (4) can be determined. As shown in Fig. 5, given the projection point $P_0(x_0, z_0)$, the left and right limit visual curves $P_0P_1P_2$ can be generated according to equations (3) and (4), respectively.



(a) Left limit visual curve (b) Right limit visual curve
 Fig. 5 Prediction for the unknown side surface

2.1.2 Top surface prediction

According to the aforementioned method in section 2.1.1, the unknown side surface can be predicted with the acquired 2.5D range image. However, the top surface of the unknown object is not taken into consideration, which may result in the 3D model being incomplete. In this section, the top surface prediction and planning

strategy around the X axis are established. As shown in Fig. 6, with the reference planar rotating around the X axis, the limit visual positions P_s and P_b are obtained. The minimal flip angle β_{is} is defined as the angle between the normal vector \vec{n}_{is} and the negative Y axis, and the maximum flip angle β_{ib} is obtained corresponding to position P_b .

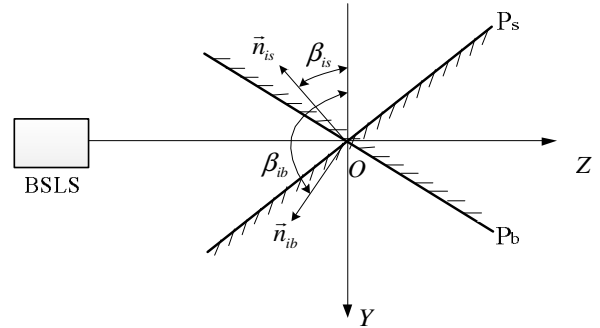
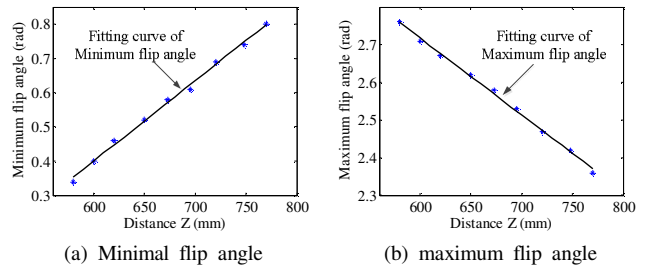


Fig. 6 The limit visual flip angle of vision system

According to the different depth z_i within DOF, a series of limit flip angles are collected (shown in Fig. 7). The corresponding formula (5) between the flip angle $\beta_{is}(\beta_{ib})(rad)$ and the depth $z(mm)$ can be determined with least squares.

$$\begin{cases} \beta_{is} = 0.0022z - 0.9086 & (570 \leq z \leq 780) \\ \beta_{ib} = -0.0021z + 3.9972 & (570 \leq z \leq 780) \end{cases} \quad (5)$$



(a) Minimal flip angle (b) maximum flip angle
 Fig. 7 Limit flip angles and the fitting curves

For the minimal flip fitting formula in equation (5), according to $\frac{\partial z}{\partial y} = \frac{\frac{\partial z}{\partial \beta_{is}}}{\frac{\partial y}{\partial \beta_{is}}} = \tan \left(\frac{\pi}{2} + \beta_{is} \right) = -\cot \beta_{is}$, the minimum and maximum flip visual curves can be obtained as equation (6), which are yielded in the same way as equations (3) and (4).

$$\begin{cases} y = 454.55 \ln (\cos (0.0022z - 0.9086)) + C_5 & (570 \leq z \leq 780) \\ y = -476.19 \ln (\cos (-0.0021z + 3.9972)) + C_6 & (570 \leq z \leq 780) \end{cases} \quad (6)$$

Given the projection center of the side surface boundary on the YOZ plane, the unknown constants C_5 and C_6 are obtained. Then, the unknown profile of the top surface can be predicted, and it provides evidence to the viewpoint planning of the top surface modeling. As shown in Fig. 8, according to the acquired projection boundaries C and A , the unknown parameters of C_5 and C_6 in equation (6) can be determined. Then, the predicted flip profiles of CD and AE are confirmed.

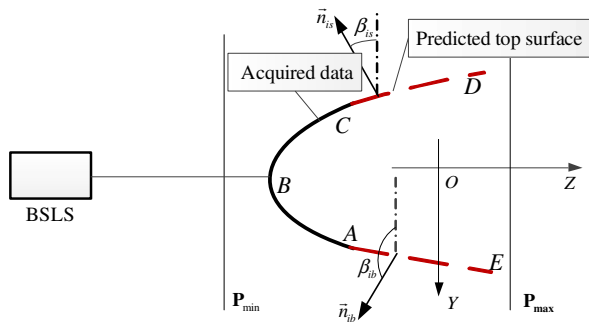


Fig. 8 Prediction for the unknown top surface

2.2 Passive vision prediction strategy

2.2.1 Shape from Shading algorithm

With the assumption of an ideal Lambertian model, SFS deals with the recovery of the 3D shape from a single gray image. Therefore, the intensity $E(x, y)$ of image $I(x, y)$ is deduced from the angle θ between the light direction and the surface normal vector, which is denoted by equation (7).

$$E(x, y) = I(x, y) \rho \cos \theta \quad (7)$$

Where ρ is the surface reflectivity of the measured object $I(x, y)$. With the surface profile $z = z(x, y)$, the discrete gradients p and q at the x and y directions are $p = \frac{\partial z}{\partial x}$ and $q = \frac{\partial z}{\partial y}$. Therefore, the ideal surface model can be denoted by equation (8).

$$E(x, y) = R(p, q) = \frac{p_s p + q_s q + 1}{\sqrt{p_s^2 + q_s^2 + 1} \cdot \sqrt{p^2 + q^2 + 1}} \quad (8)$$

The linear method²⁰ is used in this paper for its higher efficiency. In order to linearize the reflectance map in terms of z , the discrete approximations of p and q are employed by finite differences in equation (9).

$$p = \frac{\partial z}{\partial x} = z_{i,j} - z_{i,j-1}, \quad q = \frac{\partial z}{\partial y} = z_{i,j} - z_{i-1,j} \quad (9)$$

Where $i = 0, \dots, M-1$, $j = 0, \dots, N-1$, M , N are the rows and columns of an image. Substituting equation (9) to (8), the discrete Lambertian reflection model can be obtained in equation (10).

$$f(z_{i,j}) = E_{i,j} - R(z_{i,j} - z_{i,j-1}, z_{i,j} - z_{i-1,j}) = 0 \quad (10)$$

According to the Taylor expansion, we can acquire equation (11).

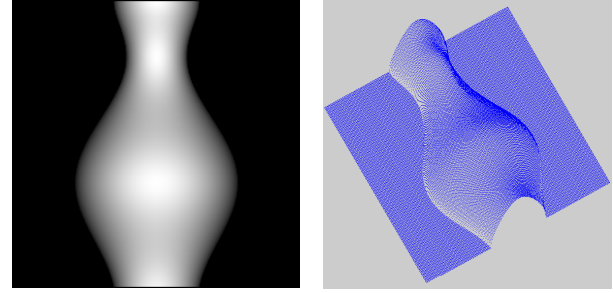
$$0 = f(z_{i,j}) \approx f(z_{i,j}^{n-1}) + (z_{i,j} - z_{i,j}^{n-1}) \frac{\partial f}{\partial z_{i,j}}(z_{i,j}^{n-1}) \quad (11)$$

With $z_{i,j}^n = z_{i,j}$, the n^{th} iteration of the result is yielded by the equation (12).

$$z_{i,j}^n = z_{i,j}^{n-1} + \frac{(-f(z_{i,j}^{n-1}))}{\frac{\partial f}{\partial z_{i,j}}(z_{i,j}^{n-1})} \quad (12)$$

$$\text{Where } \frac{\partial f(z_{i,j}^{n-1})}{\partial z_{i,j}} = -1 * \left(\frac{p_s + q_s}{\sqrt{p_s^2 + q_s^2 + 1} \cdot \sqrt{p^2 + q^2 + 1}} - \frac{(p+q) * (p * p_s + q * q_s + 1)}{\sqrt{(p^2 + q^2 + 1)^3} * \sqrt{p_s^2 + q_s^2 + 1}} \right)$$

given an initial value to the entire image with $z_{i,j}^0$, the 3D contour can be recovered by equation (12). For ideal illumination conditions, the 3D shape can be recovered from the shading image, as illustrated in Fig. 9.

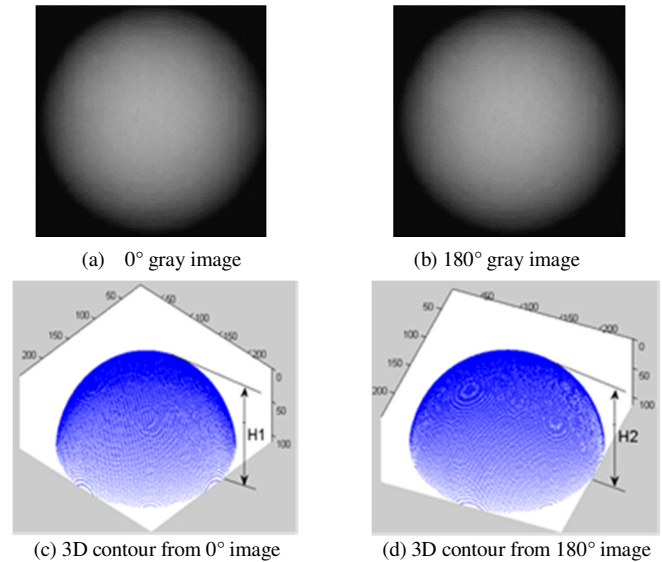


(a) Gray image of vase (b) Recovered 3D profile
Fig. 9 3D Shape recovery from a gray image of a vase

2.2.2 Boundary box dimension estimation from SFS

For a single gray image, the coarse 3D contour between 0~180° can be recovered from SFS. Therefore, with two images of the measured object captured between 180°, the entire coarse 3D size of the measured object can be determined. As shown in Fig. 10 (a) (b), the two gray images are captured by the BSLS.

With the SFS algorithm described, the coarse 3D size can be recovered from the two gray images above, as shown in Fig. 10 (c) (d). Therefore, the bounding box of the modeled object can be estimated.



(a) 0° gray image (b) 180° gray image
(c) 3D contour from 0° image (d) 3D contour from 180° image
Fig. 10 Bounding box estimation from two gray images

3. Viewpoint Planning for Automatic 3D Modeling

3.1 Viewpoint planning for automatic side surface modeling

3.1.1 Determination for the next rotation angle

Given the left rotation planning strategy for an unknown object, as shown in Fig. 11, the left projection center P_0 of a 3D contour boundary is obtained on the XOZ plane, after substituting point $P_0(x_{p0}, z_{p0})$ into equation (3), the left limit visual contour P_0P_1 can be predicted. Combined with the recovered boundary box from SFS, the left predicted contour of the unknown object can be extended to

DOI: XXX-XXX-XXXX

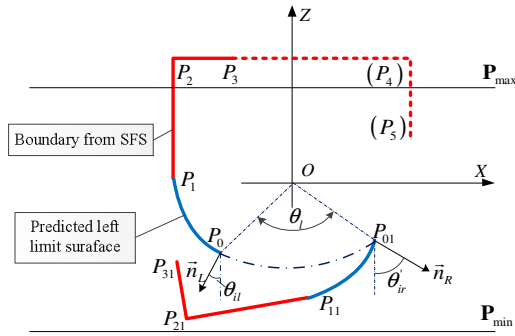
 $P_0P_1P_2P_3$.

Fig. 11 The left rotation planning schematic

When the predicted contour $P_0P_1P_2P_3$ rotates θ_l counterclockwise to $P_{01}P_{11}P_{21}P_{31}$, the left boundary center point $P_0(x_{p0}, z_{p0})$ rotates to the right limit visual position $P_{01}(x_{p01}, y_{p01})$, shown by equation (13).

$$\begin{pmatrix} x_{p01} \\ z_{p01} \end{pmatrix} = \begin{pmatrix} \cos \theta & -\sin \theta \\ \sin \theta & \cos \theta \end{pmatrix} \begin{pmatrix} x_{p0} \\ z_{p0} \end{pmatrix} \quad (13)$$

Then, substituting the point $P_{01}(x_{p01}, y_{p01})$ to the right limit visual curve in equation (2), we can acquire the right limit visual angle θ_{ir} in equation (14).

$$\theta_{ir} = \begin{cases} 0.0017(x_0 \sin \theta + z_0 \cos \theta) - 0.1382 & 570 \leq z_{01} \leq 680 \\ 1.0348 & 680 < z_{01} \leq 780 \end{cases} \quad (14)$$

At the same time, the normal vector \vec{n}_L of the boundary point P_0 changes to a new position P_{01} with \vec{n}_R , where the angle between the normal vector \vec{n}_R and z negative direction is denoted by θ_{ir}' , where

$$\theta_{ir}' = \theta_l - \theta_{il} \quad (15)$$

For the registration of the different 2.5D range image, the point P_{01} visual, the angle θ_{ir}' must be located within the right limit visual angle, therefore

$$\theta_{ir}' \leq \theta_{ir} \quad (16)$$

Finally, the critical rotated angle θ_l can be obtained by combining the three equations (14), (15) and (16), and the rotation position represents the left maximum visual surface. Similarly, the right rotation planning strategy can be carried out, and the right maximum visual surface can also be acquired with a certain rotation angle θ_r .

3.1.2 Determination of the next best viewpoint

As shown in Fig. 12, given the boundary point P_{01} after rotation, the translation range of the object can be determined with $d(d \in [z_{p01}, z_{pmax}])$. When the predicted contour $P_{01}P_{11}P_{21}P_{31}$ moves along the positive z axis, the angle θ_q at a random position of the predicted profile keeps constant while the limit visual angle changes with the depth z .

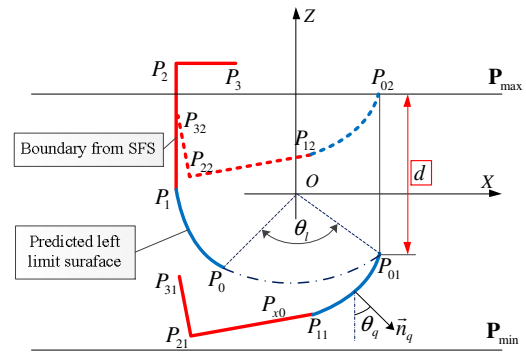


Fig. 12 Parameter schematic of the next best viewpoint

Substituting the translation d_x in the right limit visual angle equation (2), the right limit visual angle θ_{qr} can be acquired in equation (17).

$$\theta_{qr} = \begin{cases} 0.0017(z_q + d_x) - 0.1382 & 570 - z_q \leq d_x \leq 680 - z_q \\ 1.0348 & 680 - z_q < d_x \leq 780 - z_q \end{cases} \quad (17)$$

Given the limit visual condition, only the angle θ_q within the right limit visual angle, the corresponding surface patch is assumed to be visible.

$$\theta_q \leq \theta_{qr} \quad (18)$$

Therefore, combining equations (17) and (18), the critical visual position P_{x0} on the predicted contour $P_{01}P_{11}P_{21}P_{31}$ can be determined. With the predicted curves function $f_{l1}(x, z)$ obtained in equation (3), the corresponding length of the visual contour can be acquired by the curve integral in equation (19).

$$L(d_x) = \overline{P_{x0}P_{01}} = \int_{z_{p01}}^{z_{p0}} \sqrt{1 + \left[\frac{\partial f_{l1}(x, z)}{\partial z} \right]^2} dz \quad (19)$$

The visual contour length of the left translation planning can be denoted as $L(d_x)$, obtaining the maximum of $L(d_x)$ corresponding to the translation d_l , and the position parameters of the left viewpoint planning $L_{vpp} = [L_l, \theta_l, d_l]$ can be determined. And the right planning parameters $R_{vpp} = [L_r, \theta_r, d_r]$ can be obtained in a similar way. Finally, comparing the above two viewpoint parameters, the position with more visual length is deemed the next best viewpoint.

3.2 Viewpoint planning for automatic top surface modeling

According to the viewpoint planning strategy in section 3.2, the side surface can be modeled automatically. But the top surface of the measured object cannot be recovered. Therefore, the flip freedom around X is extended to achieve a complete 3D model, and the corresponding viewpoint planning strategy is illustrated as follows.

After finishing the side surface modeling, the 2.5D range image of the last side viewpoint is projected to the YOZ plane, as curve $D_0E_0F_0$ shows in Fig. 13. With the prediction of hybrid vision technology, the top predicted curve $F_0G_0H_0$ can be determined.

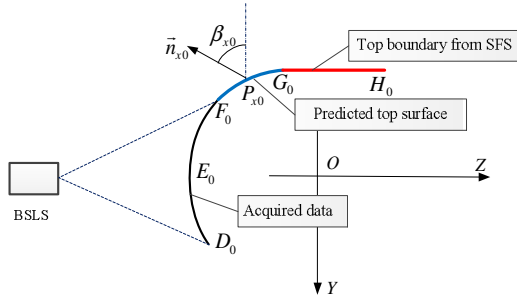


Fig. 13 Prediction of the unknown top surface

Similar to the automatic 3D modeling of the side surface, the position with maximum top predicted surface visual is assumed to be the best flip viewpoint. For the predicted curve $F_0G_0H_0$, the limit flip angle of the arbitrary point $P_{x0}(y_{x0}, z_{x0})$ is β_{x0} . Then the new position $F_1G_1H_1$ can be determined after rotating β around the X axis (as shown in Fig. 14), and the corresponding point $P_{x1}(y_{x1}, z_{x1})$ can be obtained by equation (20).

$$\begin{cases} y_{x1} = y_{x0} \cos \beta - z_{x0} \sin \beta \\ z_{x1} = y_{x0} \sin \beta + z_{x0} \cos \beta \end{cases} \quad (20)$$

The angle β_{x1} between normal vector of point $P_{x1}(y_{x1}, z_{x1})$ and negative Y axis is acquired

$$\beta_{x1} = \beta_{x0} + \beta \quad (21)$$

For the flip angle β , there are two possible conditions for further analysis.

a) When $0 < \beta \leq \pi/2$ (as shown in Fig. 14(a)), the translation range of the top surface curve $F_1G_1H_1$ is d ($d \in [z_{F1}, z_{Pmax}]$). Substituting the flipped point $P_{x1}(y_{x1}, z_{x1})$ into equation (5), the corresponding minimal flip angle β_{sx1} can be determined by equation (22):

$$\beta_{sx1} = 0.0022(y_{x0} \sin \beta + z_{x0} \cos \beta) - 0.9086 \quad (22)$$

Combining the equations (21) and (22), the critical visual point $P_{x1}(y_{x1}, z_{x1})$ in flipped curve $F_1G_1H_1$ can be obtained, thus the length L_1 of the visual part curve F_1P_{x1} among the top surface can be calculated by curve integration in equation (23).

$$L_1 = \overline{F_1P_{x1}} = \int_{z_{F1}}^{z_{P_{x1}}} \sqrt{1 + \left[\frac{\partial f_1(y, z)}{\partial z} \right]^2} dz \quad (23)$$

Thus, the maximum visual area L_{1max} can be determined with the specific position parameters (β_{1max}, d_1) .

b) When $\pi/2 < \beta \leq \pi$ (as is shown in Fig. 14 (b)), the angle β_{x1} between the normal vector of point $P_{x1}(y_{x1}, z_{x1})$ and negative Y axis is the same as in equation (21). The corresponding limit maximum flipped angle β_{bx1} can be obtained by substituting $P_{x1}(y_{x1}, z_{x1})$ into equation (5).

$$\beta_{bx1} = -0.0021(y_{x0} \sin \beta + z_{x0} \cos \beta) + 3.9972 \quad (24)$$

According to equations (21) and (24), the position of the critical point $P_{x1}(y_{x1}, z_{x1})$ can be determined, followed with the visual length L_2 of F_1P_{x1} , where

$$L_2 = \overline{F_1P_{x1}} = \int_{z_{F1}}^{z_{P_{x1}}} \sqrt{1 + \left[\frac{\partial f_2(y, z)}{\partial z} \right]^2} dz \quad (25)$$

Therefore, the maximum visual length L_{2max} with the corresponding parameters (β_{2max}, d_2) can be obtained.

c) Comparing the maximum visual length between L_{1max} and L_{2max} , the position parameters with more visual surface can be deemed the next best flip viewpoint.

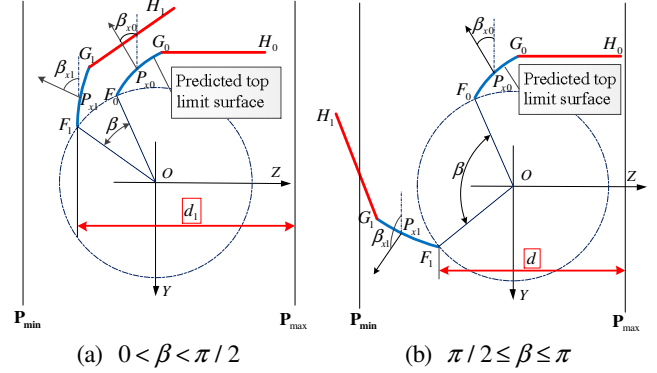


Fig. 14 The parameters for next best flip viewpoint

4. Experiments

To confirm the automatic 3D modeling method proposed in this paper, the experiment of a real object is carried out. Firstly, a gray image is acquired by the left camera of the BLS (shown in Fig. 15(a)), then another gray image is obtained from a 180° angle-interval, which is also considered as the initial viewpoint to begin 3D scanning. The 2D gray image and the 2.5D range image under the initial viewpoint are shown in Fig. 15(b) and Fig. 15(e), respectively.

The two gray images are handled by filter processing, and then the SFS technique in section 2.2 is used to recover the 3D model (shown in Fig. 15(c) and (d)), thus the coarse boundary size can be estimated, which is listed in Table 1.

Table 1 3D coarse boundary size from SFS

Recovered boundary size	$L(mm)$	$W(mm)$	$H(mm)$
	94.71	92.65	102.58

Given the 2.5D range image at the initial viewpoint, the left and right predicted curves (as shown in Fig. 15 (f)) can be determined by combining the boundary size with the limit visual surfaces. With the viewpoint planning strategy for the side surface, two candidate viewpoints are obtained and the corresponding position parameters are shown in Table 2. The next best viewpoint can be determined by comparison of the visual lengths from the two candidate positions.

Table 2 Candidate viewpoints at viewpoint1

	$\theta_l(rad)$	$d_{l1}(mm)$	$L_{l1max}(mm)$
Left candidate viewpoint	1.8248	18.2251	70.9988
	$\theta_r(rad)$	$d_{r1}(mm)$	$L_{r1max}(mm)$
Right candidate viewpoint	1.7609	21.3027	56.9760

In table 2, it is easy to note that the visual length $L_{l1max} > L_{r1max}$, which illustrates the visual surface of left planning, is greater than the right one (under the assumptions that the height of the object is constant and the length of the predicted curve is proportional to the

DOI: XXX-XXX-XXXX

area). Therefore, the left candidate viewpoint 2 (shown in Fig. 15(g)) is seemed as the next best viewpoint. Combining with the predicted curve and boundary size, the left predicted curve at viewpoint 2 (shown in Fig.15 (h)) can be yielded. Similarly, the left candidate viewpoint under viewpoint 2 can be obtained and the corresponding parameters are listed in Table 3.

Table 3 Candidate viewpoints at viewpoint 2

Left candidate viewpoint	θ_{2l} (rad)	d_{2l} (mm)	$L_{2l\max}$ (mm)
	1.8157	3.0922	81.2718

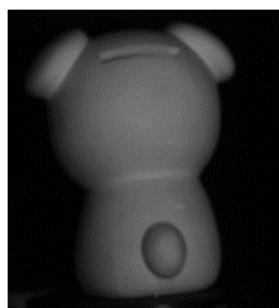
Making a comparison between the left visual surface $L_{2l\max}$ of viewpoint 2 and the right visual surface $L_{1r\max}$ of viewpoint 1, and the left visual planning of viewpoint 2 is deemed the next best viewpoint for $L_{2l\max} > L_{1r\max}$. Therefore, the viewpoint with the position parameters in Table 3 is deemed the next best viewpoint 3, and the 2.5D range image is shown in Fig. 15 (i). In addition, the viewpoint 4 (as shown in Fig. 15(k)) can be obtained in a similar way.

To ensure the integrity of the 3D model, the top surface modeling should be taken into consideration after the side surface acquisition. Given the automatic top surface modeling strategy, the top surface of the object can be predicted by the combination of boundary size and the limit flipped curve, as shown in Fig. 15 (l), and then the viewpoint parameters for the top surface modeling can be determined (illustrated in Table 4).

Table 4 Candidate viewpoint for top surface modeling

Top candidate viewpoint	β (rad)	d (mm)	$L_{up\max}$ (mm)
	1.4835	27.2098	68.2047

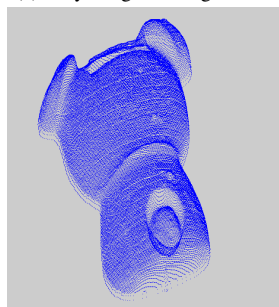
Given the parameters of the top candidate viewpoint, the 2.5D range image is obtained in Fig.15 (m). Finally, after the merging of all the 2.5D range images acquired, the complete 3D model can be obtained and the result is shown in Fig. 15 (n).



(a) Gray image at 0 degree



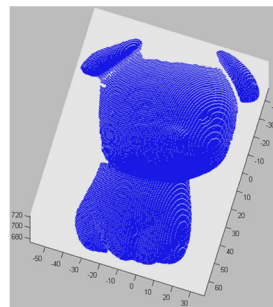
(b) Gray image at 180 degree



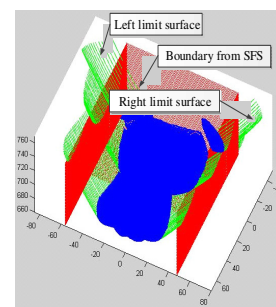
(c) 3D shape from (a)



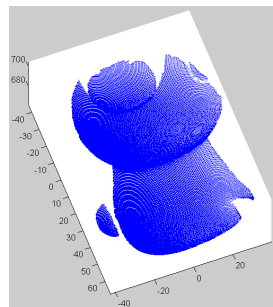
(d) 3D shape from (b)



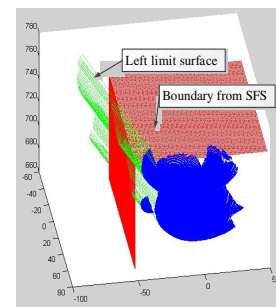
(e) Viewpoint 1



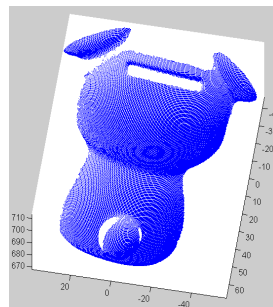
(f) Predicted curve at viewpoint 1



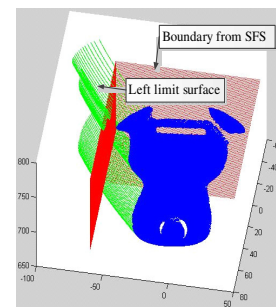
(g) Viewpoint 2



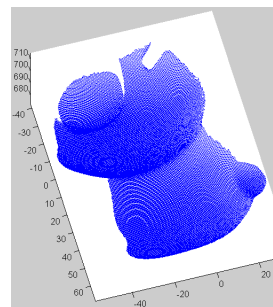
(h) Left predicted curve at viewpoint 2



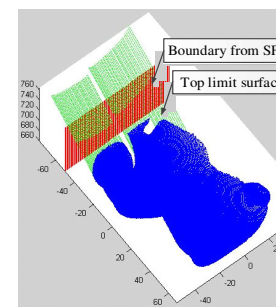
(i) Viewpoint 3



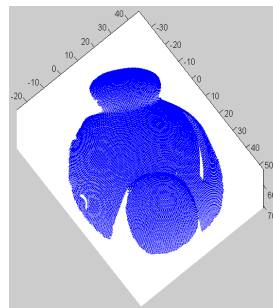
(j) Left predicted curve at viewpoint 3



(k) Viewpoint 4



(l) Top surface predicted curve



(m) Upper surface planning



(n) Final measured model

Fig. 15 Automatic 3D modeling of a dog model

5. Conclusions

This paper reviewed the research on automatic 3D modeling, and according to the widely used BSLS, a novel automatic 3D model

acquisition method based on the hybrid vision technology was proposed.

For the prediction of the unknown area, the limit visual vacuums of the BSLS are built, which can be used to estimate the unknown area from the acquired 2.5D range image. At the same time, the passive vision of SFS is deemed to be another restraint to extract the precise unknown information of the measured object. And then, with the predictions for unknown area from hybrid vision, the viewpoint planning strategy for automatic 3D modeling is carried out. To obtain the complete 3D model, the automatic planning strategy is divided into side surface and top surface reconstruction, and then the unknown 3D object can be modeled automatically and completely. The method can reduce manual intervention to a large extent. Finally, the experimental results demonstrate the effectiveness and feasibility of the proposed method.

ACKNOWLEDGMENT

The authors acknowledge the financial support of the Beijing Key Laboratory of Digital Design & Manufacture and the Digital Design and Manufacturing Engineering Research Center of Fujian Province.

REFERENCES

- Liang, C. and Wong, K., "3D reconstruction using silhouettes from unordered viewpoints," *Image and Vision Computing*, Vol. 28, No. 4, pp.579-589, 2010.
- Su, X. and Zhang, Q., "Dynamic 3-D Shape Measurement Method: A Review," *Optics & Lasers in Engineering*, Vol. 48, No. 2, pp. 191-204, 2010.
- Tong, J., Zhou J., Liu L., "Scanning 3D Full Human Bodies Using Kinects," *IEEE Transactions on Visualization & Computer Graphics*, Vol. 18, No. 4, pp.643-650, 2012.
- Hwang, S., Choi, Y., Koo, S., "Shape Reconstruction and Inspection Using Multi-planar X-ray Images," *International Journal of Precision Engineering & Manufacturing*, Vol. 15, No. 8, pp. 1545-1551, 2014.
- Nguyen, H. and Lee, B., "Laser-vision-based Quality Inspection System for Small-bead Laser Welding," *International Journal of Precision Engineering & Manufacturing*, Vol. 15, No. 3, pp. 415-423, 2014.
- Levoy, M., Pulli, K., Curless, B., et al., "The Digital Michelangelo Project: 3D Scanning of Large Statues," *Conference on Computer Graphics & Interactive Techniques*, pp. 131-144, 2001.
- Blaer, P. and Allen, P., "Data Acquisition and View Planning for 3-D Modeling Tasks," *IEEE/RSJ International Conference on Intelligent Robots and Systems*, pp. 417-422, 2007.
- Callieri, M., Fasano, A., Impoco, G., et al., "An Automatic System for Accurate and Unattended 3D Scanning," *International Symposium on 3d Data Processing, Visualization & Transmission*, Vol. 38, No. 5, pp. 805-812, 2004.
- Larsson, S., Kjellander, J.A.P., "Path Planning for Laser Scanning with an Industrial Robot," *Robotics & Autonomous Systems*, Vol. 56, No. 7, pp.615-624, 2008.
- Vasquez-Gomez, J., Sucar, L., Murrieta-Cid, R., et al., "Volumetric Next-Best-View Planning for 3D Object Reconstruction with Positioning Error," *International Journal of Advanced Robotic Systems*, Vol. 11, No. 159, pp. 1-13, 2014.
- He, B., Zhou, X., Li, Y., "The Research of An Automatic Object Reconstruction Method based on Limit Visible Region of the Laser-scanning Vision System," *Robotics and Computer-Integrated Manufacturing*, Vol. 26, No. 6, pp. 711-719, 2010.
- Torabi, L. and Gupta, K., "An Autonomous Six-dof Eye-in-hand System for in Situ 3d Object Modeling," *The International Journal of Robotics Research*, Vol. 31, No. 1, pp. 82-100, 2012.
- Martins, F.A.R., García-Bermejo, J.G., Casanova, E.Z., et al., "Automated 3D Surface Scanning based on CAD Model," *Mechatronics*, Vol. 15, No. 7, pp. 837-857, 2005.
- Sablatnig, R., Tosovic, S., Kampel, M., "Next View Planning for a Combination of Passive and Active Acquisition Techniques," *Proceedings of the Fourth International Conference on 3-D Digital Imaging and Modeling*, pp. 62-69, 2003.
- Sun, C., Tao, L., Wang, P., et al., "A 3D Acquisition System Combination of Structured-light Scanning and Shape from Silhouette," *Chinese Optics Letters*, Vol. 4, No. 5, pp. 282-284, 2006.
- Fang, W. and He B., "Automatic View Planning for 3D Reconstruction and Occlusion Handling based on the Integration of Active and Passive Vision," *2012 IEEE International Symposium on Industrial Electronics*, pp. 1116-1121, 2012.
- Kriegel, S., Rink, C., Bodenmuller, T., Suppa, M., "Efficient Next-Best-Scan Planning for Autonomous 3D Surface Reconstruction of Unknown Objects," *Journal of Real-Time Image Processing*, Vol. 10, No. 4, pp.611-631, 2015.
- Durou, J., Falcone, M., Sagona, M., "Numerical Methods for Shape-from-Shading: A New Survey with Benchmarks," *Computer Vision & Image Understanding*, Vol. 109, No. 1, pp. 22-43, 2008.
- Chang, J., Lee, K., Lee, S., "Shape from Shading Using Graph Cuts," *Pattern Recognition*, Vol. 41, No. 12, pp. 3749-3757, 2008.
- Tsai, P. and M Shah., "A Fast Linear Shape from Shading," *IEEE Computer Society Conference on CVPR*, pp. 734-736, 1992.